Chapter 6

Stabilization of metastable $LiMnO_2$ (Mn^{3+} ions) by Li-rich Li_2MnO_3 (Mn^{4+} ions): A highly efficient electro-catalyst for OER/ORR in alkaline media

In this study, different Mn-based layered compounds (γ-MnOOH, $LiMnO_2$-Li_2MnO_3, and spinel $LiMn_2O_4$) were synthesized by a cost-effective hydrothermal method and investigated as a bi-functional OER/ORR catalyst in 1M KOH aqueous electrolyte. The stabilization of metastable $LiMnO_2$ (Mn^{3+}) in Li-rich Li_2MnO_3 in the form of a composite (56% $LiMnO_2$ and 44% Li_2MnO_3) exhibited superior catalytic activity compared to the other synthesized materials. Structural characterizations such as XRD, Rietveld refinement, SAED pattern, and HR-TEM image clearly show that nanocomposite has a large number of structure defects such as ordered oxygen vacancies, resulting in stacking faults in the structure, and might be the reason behind the superior performance of composite material. Additionally, the presence of ordered oxygen-vacant sites may lead to the formation of terminal hydroxyl and Mn^{3+}-di-μ-oxo-Mn^{4+} complexes, which further enhance the catalytic activity of the composite material. Our study reveals the stabilization of Mn^{3+} in a layered composite coupled with ordered oxygen vacancies provides a promising avenue for the development of a new class of Mn-based electrocatalyst for efficient water oxidation.

6.1 Introduction

Water oxidation is generally considered to be the bottleneck reaction in artificial photosynthesis [210]–[213]. In electrochemical water splitting, hydrogen is produced at the cathode, and oxygen is evolved at the anode. The anodic oxygen evolution reaction (OER) can be utilized in a variety of energy applications, including solid oxide fuel cells, metal-air batteries, and water electrolyzers [214][215]. However, the process of water oxidation is thermodynamically unfavorable and involves a multi-step charge-transfer reaction pathway [216], therefore requiring a large amount of energy input to drive the reaction.

$$2H_2O \rightarrow O_2 + 2H_2$$

$$2H_2O \rightarrow 4H^+ + 4e^- + O_2$$

$$4H^+ + 4e^- \rightarrow 2H_2$$

$$E^0(O_2/H_2O) = 1.23\ V\ vs\ RHE$$

The thermodynamic potential required for water electrolysis is 1.23 V, however, most of the widely employed electrocatalysts exhibited large overpotential for OER reaction [217]. Although noble metal-based oxides (such as IrO_2 and RuO_2) have been investigated as the most effective catalysts for oxygen evolution reactions (OER), their practical application is limited by their high cost, scarcity, and instability in alkaline electrolytes [218]. In naturally occurring photosystem-II (PS-II), the water oxidation reaction proceeds with high catalytic activity due to the formation of μ-oxo bridged tetrameric Mn-cluster (Mn_4CaO_5) within the complex protein environment [219]–[221]. Thus, the Mn-clusters of photosynthetic organisms have triggered extensive research efforts to develop efficient Mn-based water oxidation catalysts [211][221]–[224]. The catalytic activities of manganese oxides heavily depend on their chemical compositions and crystallographic phases [83][97][225]. Manganese oxides have been found in more than 20 polymorphs, and their multivalent nature and nonstoichiometric composition make them more complicated than other metal oxides [211]. Previously, manganese oxides deposited through electrochemical cycling exhibited remarkable bi-functional OER/ORR activities in an alkaline medium (0.1 M KOH). The authors attributed this phenomenon to the formation of Mn^{3+}/Mn^{4+} redox couple, which is accompanied by the

potential bias during electrolysis [226]. Bergmann et al. established a relationship between structures and activities by comparing the OER activity of δ-MnO_2 (layered) and β-MnO_2 (tunneled). The tunneled structures exhibited higher intrinsic OER activities compared to the layered materials due to improved water accessibility and the presence of defects in the systems [227]. In another study, Najafpour et al. found that the unique structural motifs such as structural defects (low order), di-μ-oxo bridging sites, and mixed valence state of Mn (20% Mn^{III}/Mn^{IV}, average oxidation state = 3.8) played a crucial role [228][229] for an efficient water electrolysis process.

Dismukes et al. showed that the OER activity of MnO_2 polymorphs is greatly enhanced when Mn^{3+} ions are present in the lattice [228][230]. Computational investigations, supported by extended X-ray absorption fine structure (EXAFS) study, clearly demonstrate that the Mn^{3+} ions occupy a tetrahedral environment that is kinetically stable and creates localized strain within the lattice. This strain causes the O 2*p* valence band to elevate above the Mn^{3+} tetrahedral (td) and Mn^{4+} octahedral (oh) valence bands, resulting in a decrease in metal conduction bands. Consequently, the oxidation of tetrahedral Mn^{3+} becomes more challenging compared to that of oxygen, leading to an enhancement of the OER performance of the catalysts. Recently, multiple reports have highlighted a correlation between the content of Mn^{3+} and the catalytic activity of oxygen evolution reaction (OER) [231]–[234]. Therefore, any strategies aiming to enhance the activity of manganese oxides must focus on the stabilization of Mn^{3+} to prevent its disproportionation into inactive Mn^{4+} and Mn^{2+} species.

$$2MnOOH + 2H^+ \leftrightarrow MnO_2 + Mn^{2+} + 2H_2O$$

Several studies have shown that layered [235]–[238] and lithiated spinel-type $LiMO_2$ (M = Ni, Co, Fe, Mn) exhibited excellent OER activity in alkaline electrolytes. One of the interesting and most technologically relevant characteristics of these materials is that the lithium content can be varied, which can be utilized as a tool to tune the oxidation state of the transition-metal ions. Therefore, an optimized ratio of M^Z/M^{Z+1} in the layered compound caused by lithiation/delithiation produces a lot number of ordered oxygen vacancies and structure faults in the crystal, which may act as an efficient oxygen evolution center for water oxidation.

In the current study, we have synthesized various Mn-based electrocatalysts, including γ-MnOOH, $LiMnO_2$-Li_2MnO_3, and spinel $LiMn_2O_4$, using a two-step hydrothermal method. Characterization techniques such as X-ray diffraction (XRD), Rietveld refinement analysis, selected-area electron diffraction (SAED), high-resolution transmission electron microscopy (HRTEM), and Raman spectroscopy reveal that a large number of structural defects such as oxygen vacancies and stacking faults are present in $LiMnO_2$-Li_2MnO_3 nanocomposite. Further, the stabilization of metastable $LiMnO_2$ (Mn^{3+}) in Li-rich Li_2MnO_3 in the form of a composite (56% $LiMnO_2$ and 44% Li_2MnO_3) exhibited superior electrochemical performance towards OER/ORR in aqueous 1M KOH electrolyte compared to the other synthesized materials. We have shown that the stabilization of Mn^{3+} in a layered composite coupled with ordered oxygen vacancies in terms of stacking faults provides a promising avenue for the development of a new class of Mn-based electrocatalysts, which have significantly low overpotential for water oxidation.

6.2 Experimental

6.2.1 Materials synthesis

6.2.1.1 Synthesis of γ-MnOOH

1.4 g of $KMnO_4$ (98.5%) and 1 g of cetyltrimethylammonium bromide (99%) were dissolved in 70 mL of double distilled water and stirred for an hour. Afterward, the solution was transferred into a 100 mL autoclave, sealed, and heated at a temperature of 180 °C for a duration of 12 hours. The autoclave was then allowed to cool down to room temperature. The resulting material was washed several times with ethanol and distilled water, followed by drying at 70 °C to produce phase pure γ-MnOOH nanorods.

6.2.1.2 Synthesis of $LiMnO_2$-Li_2MnO_3 nanocomposite and $LiMn_2O_4$

6.0 g of LiOH .H_2O (99%) and 1 g of the prepared γ-MnOOH nanorods were dissolved in 70 mL of water. After stirring for 30 minutes, the mixture was transferred into a 100 mL autoclave and heated at 200 °C for 12 hours. The resulting product was washed with ethanol and distilled water multiple times and then dried at 70 °C to obtain the $LiMnO_2$-Li_2MnO_3 nanocomposite. To synthesize the spinel $LiMn_2O_4$ nanorods, the $LiMnO_2$-Li_2MnO_3 nanocomposite was subjected to calcination at 400 °C for 4 hours in a nitrogen atmosphere.

6.2.2 Material characterizations

The crystallinity and phase identification of prepared materials were confirmed by the powder XRD method using a Rigaku Miniflex X-ray diffractometer with Cu Kα radiation (λ = 1.54 Å) in the 2θ range of 10–80° and a step size of 0.02° at a scan rate of 2° min^{-1}. The structure was refined by a two-phase Rietveld refinement method using FULLPROF suite software. To investigate the electronic structures of the materials, XPS studies were conducted using a Thermo Scientific Multilab 2000 instrument operated at 150 W and employed Al Kα as the radiation source. All binding energy values were charge-corrected by referencing C 1*s* spectra located at 284.5 eV. Peak deconvolution was performed using XPSPEAK41 software. Raman spectra were collected using an inVia micro-Raman spectrophotometer (Renishaw). The instrument uses an argon ion laser source with a wavelength of 532 nm and a power output of 10 mW. The wave number range for the spectra was 200 to 800 cm^{-1}. Scanning electron microscopy (EVO-Scanning Electron Microscope MA15/18) equipped with Energy-dispersive X-ray spectroscopy was used to analyze the microstructure, morphology, and elemental mapping of the synthesized materials. High-resolution transmission electron microscopy (HR-TEM) images were obtained using an FEI TECNAI G2 20 TWIN microscope operating at 300 kV to measure the lattice spacing. The surface area (SA) analysis based on the Brauer-Emmett-Teller (BET) method was conducted using a MicrotracBEL instrument. The analysis is carried out in an N_2 atmosphere at 77.3 K.

6.2.3 Electrode fabrication for electrochemical measurements

All the electrochemical measurements were performed with the help of an electrochemical workstation based on a Pine research instrument (Wave driver 200). The setup consisted of a three-electrode system: a catalyst-loaded carbon paper (1 cm^2) as the working electrode, Ag/AgCl/4M KCl as the reference electrode, and a platinum wire as the counter electrode. To obtain a homogeneous catalyst ink, 20 mg of the catalyst sample, 5 mg of activated carbon, and 5 µl of Nafion binder were sonicated in 1 ml of N-methyl pyrrolidone (NMP) for 30 minutes. The resulting ink was then deposited on carbon Toray paper and dried at 80 °C for 12 hours in a vacuum oven. The mass of the active material loaded on the substrate was approximately 1 mg cm^{-2}. Electrochemical analysis was performed using the Aftermath software, which involved linear sweep voltammetry, cyclic

voltammetry, and electrochemical impedance spectroscopy in O_2 saturated 1 M KOH electrolyte. Freshly prepared electrolyte solutions were used for each set of experiments, consisting of analytical grade KOH (Merck, 85%) and deionized water. All potentials were reported relative to the reversible hydrogen electrode (RHE). To convert the obtained potential (vs. Ag/AgCl) to the RHE, the following equation was employed:

$$E_{RHE} = E_{Ag/AgCl} + 0.059\,pH + E^0_{Ag/AgCl} \ldots\ldots (6.1)$$

Where, $E^0_{Ag/AgCl}$ (in 4 M KCl) = + 0.199V; pH = 13.8 for 1 M KOH.

6.3 Results and discussion:

6.3.1 Crystal structure and Morphology

Fig. 6.1(a), (b), and (c) show the XRD, SEM, and high-resolution TEM images of the γ-MnOOH precursor prepared by the reduction of Mn^{7+} ($KMnO_4$) to Mn^{3+} (MnOOH) using CTAB as a reducing agent in a hydrothermal process. All the diffraction peaks in the pattern (Figure 6.1a) can be well indexed to monoclinic γ-MnOOH (JCPDS 41-1379), demonstrating the high purity of the precursor. SEM image of γ-MnOOH (Figure 6.1b) shows that the material consisted mainly of uniform nanorods with typical diameters in the range of 200 to 300 nm and lengths of up to several micrometers. In the high-resolution TEM image (Figure 6.1c), the lattice fringes of the nanorods can be seen. From the image, the distance between adjacent lattice planes can be measured to 0.34 nm which corresponds to the (11-1) planes of the monoclinic γ-MnOOH.

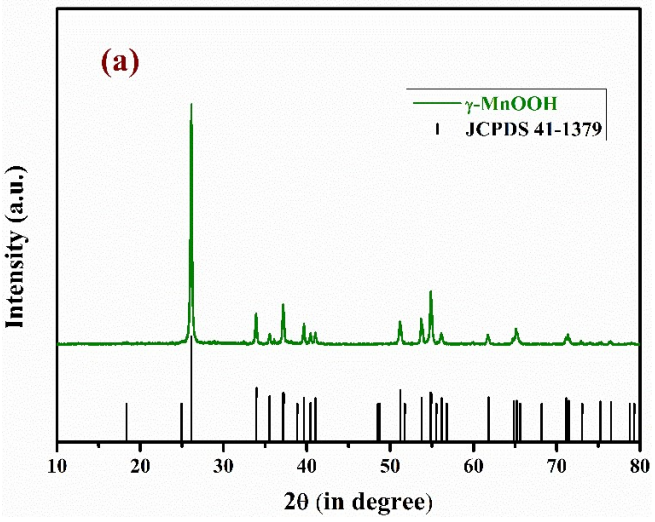

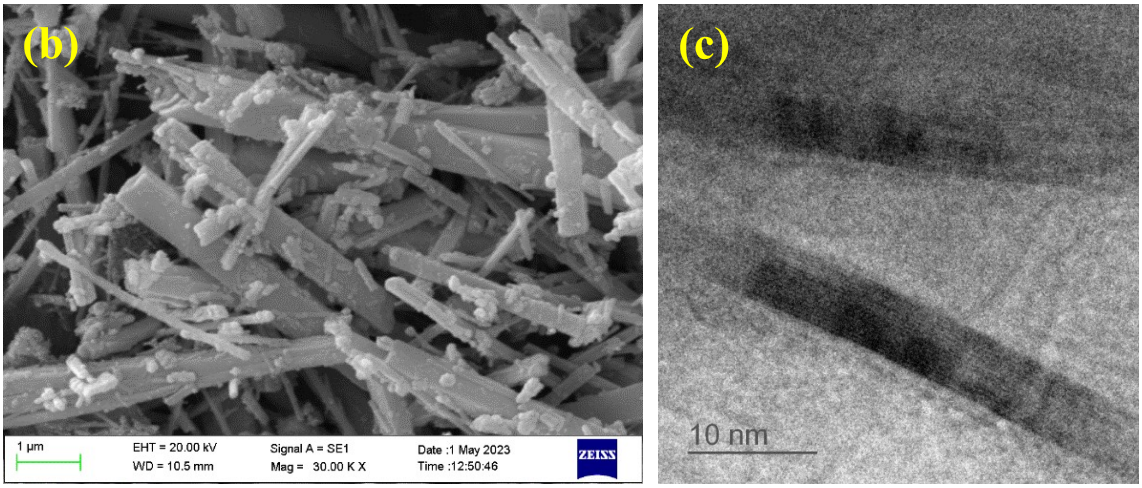

Figure 6.1: shows the (a) XRD, (b) SEM, and (c) high-resolution TEM images of the γ-MnOOH

Fig. 6.2(a) shows the XRD pattern of $LiMnO_2$-Li_2MnO_3 nanocomposite obtained after the hydrothermal treatment. The XRD pattern of $LiMnO_2$-Li_2MnO_3 nanocomposite shows mixed phase formation; one phase corresponds to the orthorhombic $LiMnO_2$ (JCPDS 035-0749), while the other shows the monoclinic phase of Li_2MnO_3 (JCPDS 027-1252). The diffraction peaks observed at 15.4°, 24.9°, 35.5°, 36.8°, 37.6°, 39.4°, 40.8°, 42.5°, 45.1°, 61.4°, and 65.5° are attributed to the (010), (110), (011), (120), (101), (200), (111), (210), (021), (221) and (002) planes of orthorhombic $LiMnO_2$, whereas diffraction peaks appeared at 18.5°, 22.7°, 44.7°, 48.8°, 58.6°, and 65.4° correspond to the (010), (-111), (-133), (133), (135), and (060) planes of monoclinic Li_2MnO_3. Furthermore, the phase fraction analysis of $LiMnO_2$-Li_2MnO_3 nanocomposite was carried out with the help of the two-phase Rietveld refinement method. The structural refinement was based on the layered $Li_{2/3}[Li_{1/3}Mn_{2/3}]O_2$ having space group C2/c and $LiMnO_2$ having space group Pmnm, respectively. Fig. 6.2b shows the Rietveld refinement XRD pattern for $LiMnO_2$-Li_2MnO_3 nanocomposite and Table 6.1, summarizes the R factors, lattice parameters, and final structure parameters determined through the Rietveld analysis. For $LiMnO_2$-Li_2MnO_3 nanocomposite, the profile fittings provide a compound composition to be 56% orthorhombic $LiMnO_2$ and 44% monoclinic Li_2MnO_3. Interestingly it was noticed that the occupancy parameters at the oxygen 2b sites for O1 and O2 in the orthorhombic phase $LiMnO_2$ is 1.0, whereas it is found to be 0.785 for

monoclinic phase Li_2MnO_3. Therefore, a large amount of oxygen vacancies exists in the monoclinic phase of Li_2MnO_3, acting as an OER center for the catalyst, while no oxygen vacancies were found in the orthorhombic phase of $LiMnO_2$ in the composite.

Table 6.1: Structural Parameters of $LiMnO_2$-Li_2MnO_3 composite based on Rietveld Refinement

Catalyst	Phases	Lattice parameter			Vol^m	Reliability factors			Contribution
						R_f	R_{Bragg}	χ^2	
$LiMnO_2$-Li_2MnO_3 composite	$LiMnO_2$ (Pmnm)	a=2.81(4)	b=5.75(9)	c=4.58(6)	74.07	2.26	1.96	2.38	0.56
		α=90	β=90	γ=90					
	Li_2MnO_3 (C2/c)	a=4.93(2)	b=8.55(4)	c=9.58(3)	398.37	1.85	1.86	2.38	0.44
		α=90	β=99.23(4)	γ=90					

As shown in Fig. 6.2c, the $LiMnO_2$-Li_2MnO_3 nanocomposite prepared from γ-MnOOH retains the rod-like morphology of the precursor even though the reaction was carried out at high temperature (200 °C) and strong alkali medium. An overview of the SEM image (Fig. 6.2d) shows that the $LiMnO_2$-Li_2MnO_3 nanorods were interconnected to form a porous network architecture. Fig. 6.2e shows the area of the sample on which EDX mapping was carried out to get the elemental uniformity and composition of the material. Fig. 6.2 (f-g) shows the different elemental color mapping of Mn, and O atoms. Since the excitation energy of the Li element is low, it is not possible to detect Li in the sample by SEM−EDX. The energy-dispersive spectra confirm only the presence of Mn and O atoms.

To confirm that two different crystal structures coexist in $LiMnO_2$-Li_2MnO_3, we characterized the material with high-resolution TEM images. Fig. 6.3a shows the bright field TEM images of the nanocomposite, with its corresponding selected area electron diffraction pattern, shown in Fig. 6.3b. Figure 6.3c shows the high-resolution TEM of $LiMnO_2$-Li_2MnO_3 nanocomposite, which denotes the high density of stacking faults present in the structure.

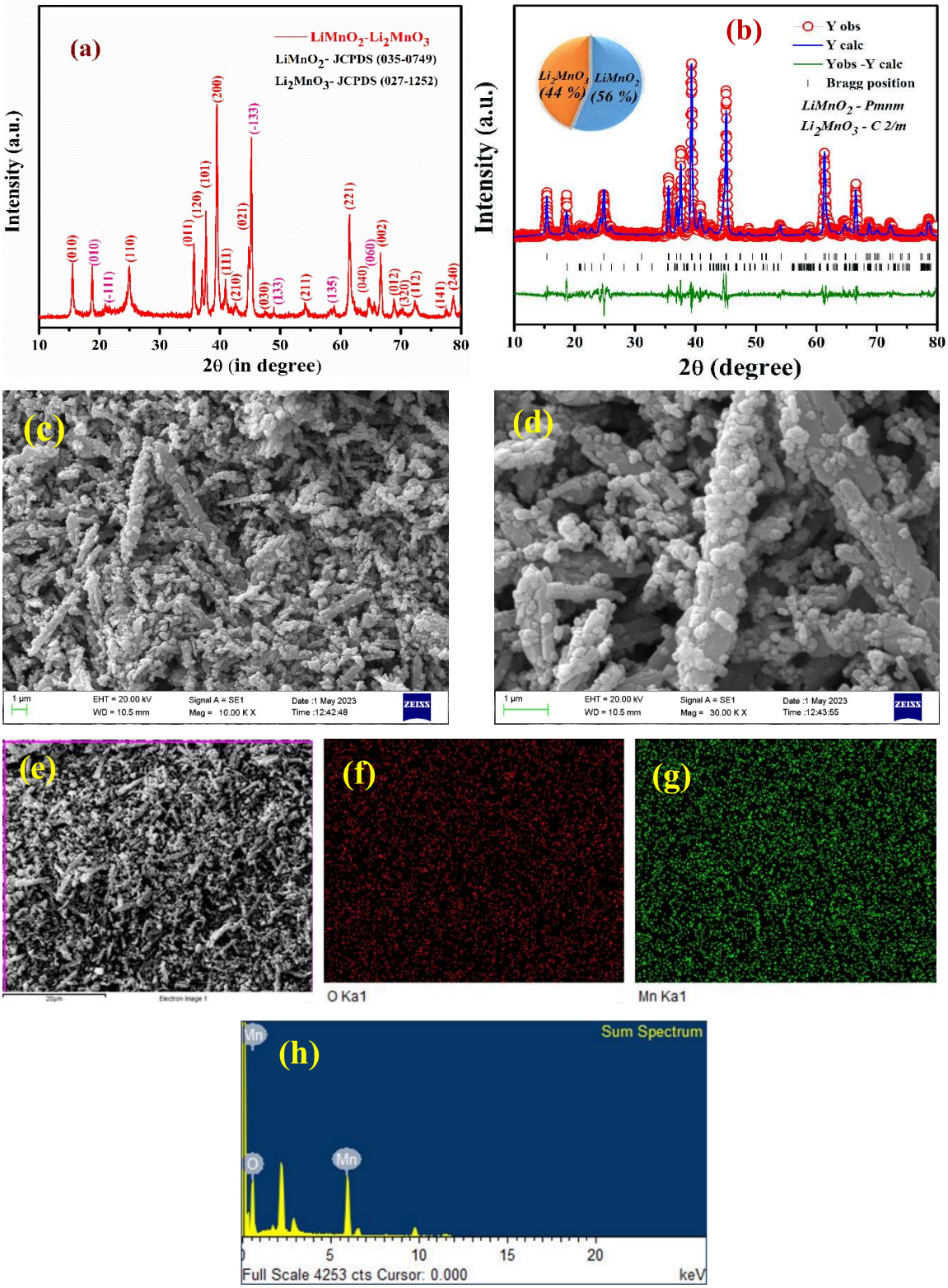

Figure 6.2: (a) XRD pattern, (b) Rietveld refinement study, (c), (d) SEM and (e-h) EDAX analysis with spectrum of $LiMnO_2$-Li_2MnO_3 nanocomposite.

To see the stacking faults more clearly, areas A, B, and C in Fig. 6.3c are enlarged and shown in the right panels of Fig. 6.3c (the inset show the inverse FFT image of area A, B, and C). A high density of stacking faults leads to quite different interplanar spacing for the same lattice planes. For example, the interplanar distances of the (001) lattice planes are measured to be 0.505, 0.489, and 0.472 nm, respectively. These high-resolution TEM images show that reduction in a strongly alkaline medium at 200 °C produces a large number of ordered oxygen vacancies resulting in stacking faults in the structure.

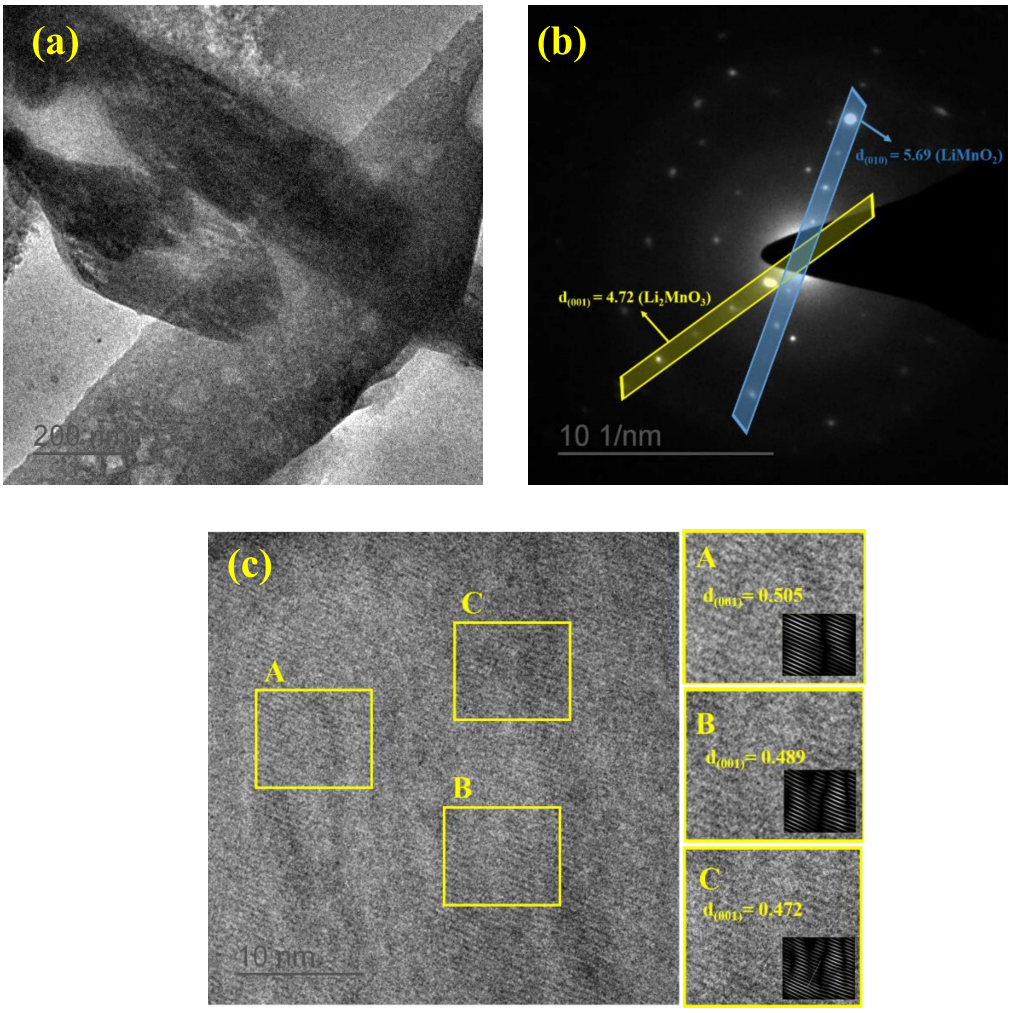

Figure 6.3: (a) Bright-field TEM images, (b) SAED pattern, and (c) high-resolution TEM image of $LiMnO_2$-Li_2MnO_3 nanocomposite (inset show the inverse FFT image of area A, B, and C).

6.3.2 Raman and Surface area analysis

Raman spectrum has been measured to probe the oxygen environments around the lithium and manganese cations in $LiMnO_2$-Li_2MnO_3 nanocomposite, shown in Figure 6.4a. In the Raman spectrum, there are nine well-resolved peaks, in the range of 200–800 cm^{-1}. These nine peaks were explained and assigned to the Li–O stretching vibrations of LiO_6 octahedrons and Mn–O stretching vibration of MnO_6 octahedrons in monoclinic Li_2MnO_3, respectively, by Julien and Massot [239]. Additionally, a characteristic broad and overlapping peak in 550–700 cm^{-1} is observed, which is associated with the strongest Mn–O bonds arising due to oxygen deficiency of Li_2MnO_3. This characteristic broad and overlapping peak can be fitted into four peaks, located at 580, 605, 632, and 658 cm^{-1}, respectively. These fitted peaks have almost the same frequencies as in the Raman spectrum of orthorhombic $LiMnO_2$ [240].

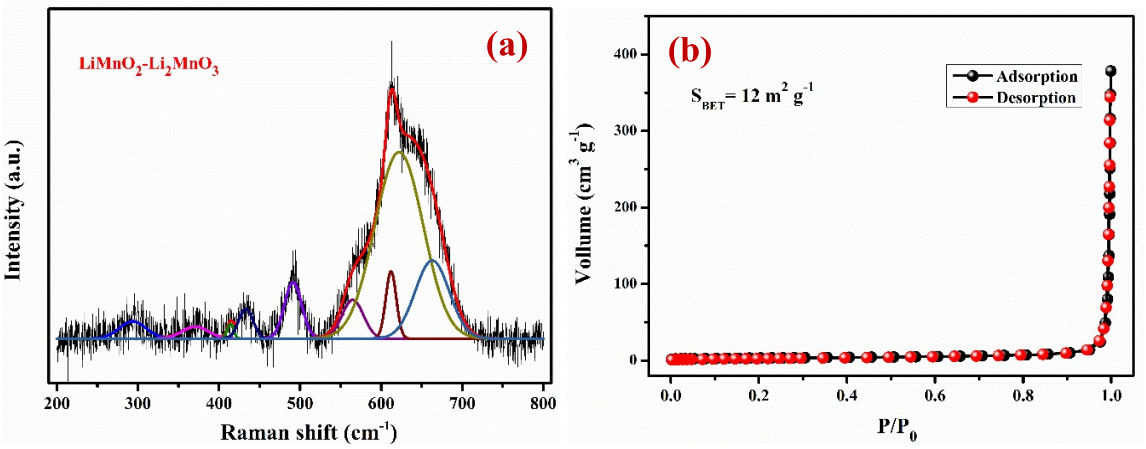

Figure 6.4: (a) Raman spectra and (b) BET surface area analysis of $LiMnO_2$-Li_2MnO_3 nanocomposite

6.3.3 XPS analysis

The XPS measurements were performed to analyze the electronic structure of the materials and study the oxidation state of the elements (Li, Mn, and O) present in the nanocomposite. Figure 6.5a shows the core level XPS spectra of Mn 2*p* that can be attributed to the spin-orbit doublet of Mn 2*p*3/2 and Mn 2*p*1/2. Further, these two broad peaks can be well-fitted into four peaks. Two peaks, located at 642.1 and 656.0 eV, are attributed to the

Mn^{3+} state, whereas the other two peaks located at 642.6 and 653.6 eV could be assigned due to the presence of the Mn^{4+} state. The spin-orbital separation of Mn 3*s* peaks equivalent to 4.92 eV, shown in Figure 6.5b, verifies the presence of Mn^{3+} and Mn^{4+} in the nanocomposite. Further, the relative concentration of $LiMnO_2$ and Li_2MnO_3 in the composite was determined by the ratio of the Mn^{3+}/Mn^{4+} peaks. The core level spectra of Li 1*s* given in Figure 6.5c, have two binding energy values one at ~54.5 and another at ~55.9 eV, which indicates that lithium is present in two different cationic environments (LiO_6 octahedral and intermixing of LiO_6 octahedral in MnO_6 layer, respectively). Further, the deconvoluted O 1*s* spectra consist of three peaks centered at ~529.4 ~531.2, and 532.8 eV (Fig. 6.5d), confirming the presence of Mn-O-Mn, Mn-OH, and adsorbed H_2O, respectively. The relative surface concentrations of Li/Mn were measured by integrating the intensities of Mn 2*p* and Li 1*s* peaks using the following formula [241].

$$Relative\ concentration, C_M = \frac{I_M / \lambda_M \sigma_M D_M}{\sum \left(I_M / \lambda_M \sigma_M D_M \right)} \ldots\ldots (6.2)$$

where I_M is the integrated intensity of the core levels (M = Mn 2*p*, and Li 1*s*), λ_M is the mean escape depth of the respective photoelectrons, σ_M is the photoionization cross-section, and D_M is the geometric factor. The photoionization cross-section values were taken from Scofield's data [242], and the mean escape depths were taken from Penn's data. The geometric factor was taken as 1 because the maximum intensity in this spectrometer was obtained at 90°. The relative surface concentrations of Li: Mn were found to be 3:2 in $LiMnO_2$-Li_2MnO_3 nanocomposite. Thus, the combined XRD and XPS studies confirm the formation of a large number of oxygen vacancies and stacking faults in the layered $LiMnO_2$-Li_2MnO_3 nanocomposite.

Furthermore, when $LiMnO_2$-Li_2MnO_3 nanocomposite was subjected to calcined at 400 °C under N_2 atmosphere, the layered-structured transformed to spinel-$LiMn_2O_4$. Figures 6.6a and 6.6b show the XRD and SEM images of spinel-$LiMn_2O_4$. The diffraction pattern of $LiMn_2O_4$ indexed to the cubic phase having space group Fd3m (PDF No. 01-082-0321). SEM image of $LiMn_2O_4$ clearly shows calcination treatment does not affect the rod-like morphology of the prepared materials.

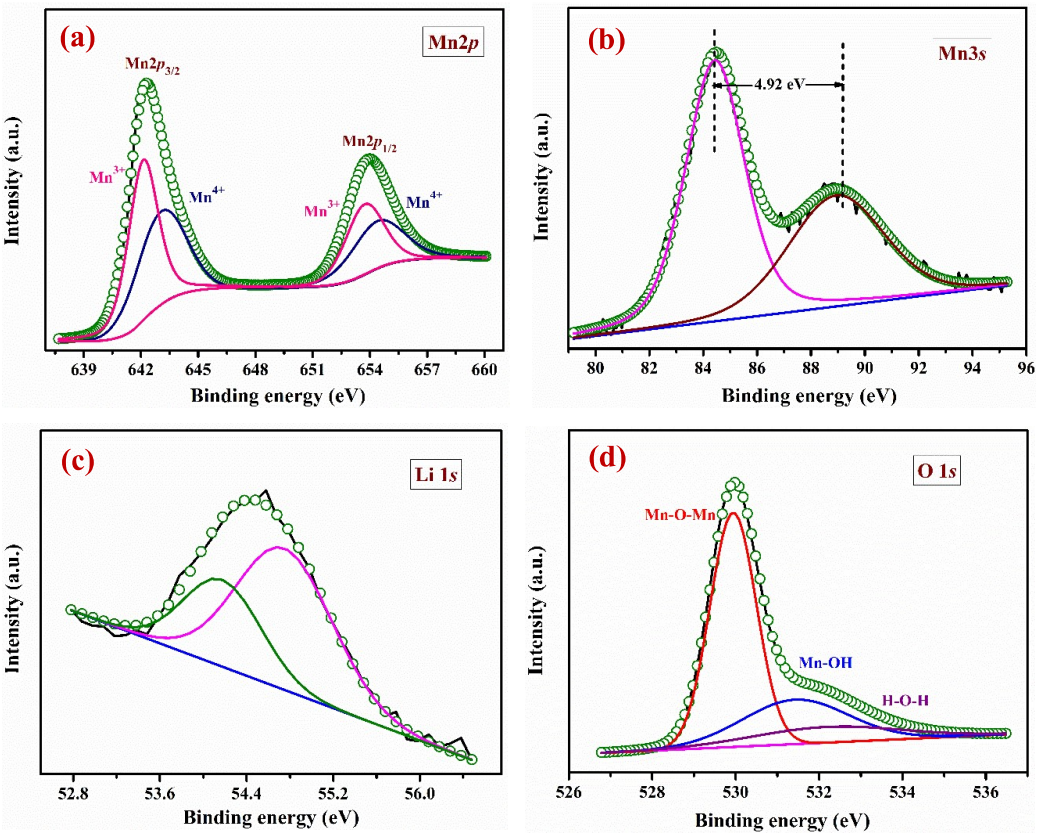

Figure 6.5: (a) the variation of Mn^{3+} and Mn^{4+} in $LiMnO_2$-Li_2MnO_3, (b) the core level XPS spectra of Mn 3s, (c) Li 1s, and O 1s in $LiMnO_2$-Li_2MnO_3 nanocomposite.

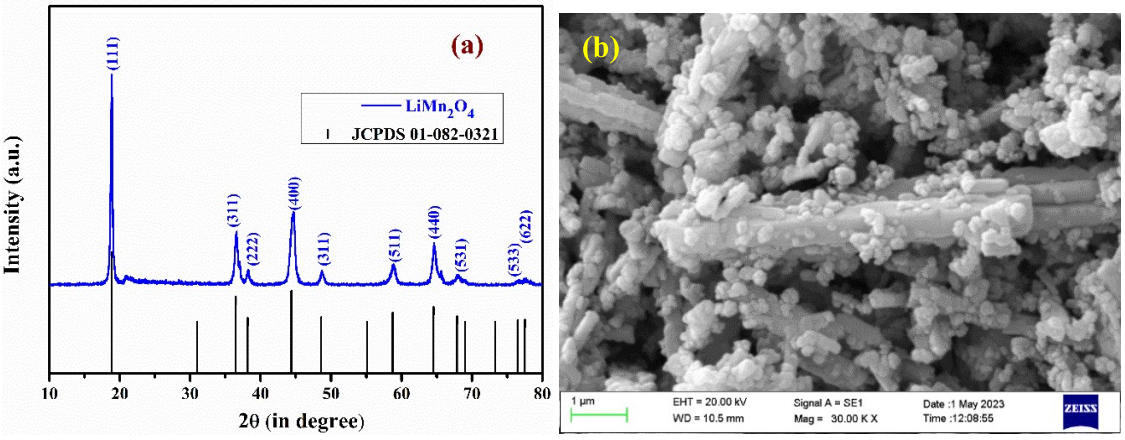

Figure 6.6: shows (a) XRD and (b) SEM images of $LiMn_2O_4$ obtained after the heat treatment.

6.3.4 Electrochemical Study:

The electrochemical performance of prepared electrocatalysts (γ-MnOOH, $LiMnO_2$-Li_2MnO_3, and $LiMn_2O_4$) toward the OER was investigated in O_2-saturated 1 M KOH at a scan rate of 5 mV s^{-1} in a three-electrode setup. Before collecting the data, the working electrode was first scanned for several cycles at a scan rate of 100 mV s^{-1} in the range of 1.0-1.8 V versus the RHE to obtain a stable current. The LSV curves, shown in Figure 6.7a, represent the OER performance of all the synthesized catalysts, which follow the order $LiMn_2O_4$ < γ-MnOOH < $LiMnO_2$-Li_2MnO_3. Figure 6.7(b) shows the ORR activity of the prepared samples, and they follow similar features as OER. It was observed that at the potential of 0.9 V vs. RHE the catalysts $LiMn_2O_4$, γ-MnOOH, and $LiMnO_2$-Li_2MnO_3 exhibited 1.77, 3.68, and 6.55 mA cm^{-2} current density, respectively.

$$O_2 + 2H_2O + 4e^- \rightarrow 4OH^-$$

For the OER activity, the required overpotential to achieve a current density of 10 mA cm^{-2} (based on 10% solar-to-fuel conversion efficiency) for γ-MnOOH, $LiMnO_2$-Li_2MnO_3, and $LiMn_2O_4$, was found to be 382, 316, and 492 mV, respectively, shown in Figure 6.7c. Figure 6.7d shows the Tafel plot of various synthesized catalysts, and the slope values obtained for γ-MnOOH, $LiMnO_2$-Li_2MnO_3, and $LiMn_2O_4$ are approximately 108, 82, and 158 mV dec^{-1}, respectively. The lowest Tafel slope of $LiMnO_2$-Li_2MnO_3 (82 mV dec^{-1}) indicates its much faster reaction kinetics among all the catalysts. Furthermore, the impedance studies were conducted in the frequency range of 0.1 Hz to 100 kHz at a potential of 1.5 V versus RHE with an AC amplitude of 10 mV to measure the charge-transfer resistance of catalysts, as shown in Figure 6.7f. An equivalent circuit fit of the EIS data is also given in the inset of Figure 6.7f. The Nyquist semicircle loop diameter at the high-frequency region represents the charge-transfer resistance (R_{ct}), an important parameter that decides the superiority of a catalyst for the OER process. The stabilization of metastable $LiMnO_2$ (Mn^{3+}) in $LiMnO_2$-Li_2MnO_3 composite can significantly reduce the R_{ct} value that follows the order $LiMn_2O_4$ > γ-MnOOH > $LiMnO_2$-Li_2MnO_3. The lowest R_{ct} value of $LiMnO_2$-Li_2MnO_3 (27 Ω) indicates its much faster charge-transfer kinetics during the catalytic process among all the catalysts.

In the present study, commercial RuO_2 (Sigma-Aldrich) was tested as a reference catalyst under the same experimental conditions. Figure 6.7e presents the LSV curves of RuO_2 along

with $LiMnO_2$-Li_2MnO_3 to compare their OER performance in 1 M KOH. From Figure 6.7e, we observe that RuO_2 requires 344 mV overpotential to reach a current density of 10 mA cm^{-2}, whereas to achieve the same current density, $LiMnO_2$-Li_2MnO_3 takes only a 316 mV overpotential. The Tafel slope value of RuO_2 is 93 mV dec^{-1} (Fig. 6.7d) which is larger than $LiMnO_2$-Li_2MnO_3 (82 mV dec^{-1}) and in accordance with the OER performances because a lower Tafel slope represents a faster OER kinetics. The activity of commercial RuO_2 provides in the present study is in close agreement with their earlier reports. The impedance spectra of $LiMnO_2$-Li_2MnO_3 and commercial RuO_2 were also measured at a potential of 1.5 V vs RHE, shown in Figure 6.7f. The R_{ct} value of RuO_2 is found to be 48.56 Ω, which is quite larger than $LiMnO_2$-Li_2MnO_3 (27 Ω), indicating its faster OER kinetic rate than the RuO_2 reference catalyst.

Fig. 6.4b presents the BET surface area measurement (N_2 adsorption/desorption isotherms) of $LiMnO_2$-Li_2MnO_3, and from the isotherm, the specific SA of $LiMnO_2$-Li_2MnO_3 is found to be 12 m^2 g^{-1}, while it is 11.38 m^2 g^{-1} for commercial RuO_2 [42]. Furthermore, the electrochemically active surface area (ECSA) of the catalysts along with RuO_2 was estimated by measuring the electric double-layer capacitance in the non-Faradaic region at various scan rates from 5 to 50 mV/sec through cyclic voltammetry. The double-layer capacitance (C_{dl}) of RuO_2 and the other synthesized catalysts was shown in Figure 6.8a. For a better understanding of the intrinsic OER activity, the ESCA normalized current density of different catalysts was calculated and depicted in Figure 6.8b. The ECSA normalized OER activities of the catalysts also confirmed the best performance for $LiMnO_2$-Li_2MnO_3 (Fig. 6.8c). A similar trend was also observed for the number of active sites of the different catalysts shown in Fig. (6.8d) and (6.8e). The highest number of active sites (27.7×10^{16}) was calculated for $LiMnO_2$-Li_2MnO_3. The turnover frequencies (TOFs) of the different catalysts were also calculated and found to be the highest for $LiMnO_2$-Li_2MnO_3 (TOF = 0.28 s^{-1}). Therefore, the superior OER activity of $LiMnO_2$-Li_2MnO_3 over other synthesized catalysts has been established in terms of the number of active sites, overpotential, TOF, and ECSA normalized current density, shown in Table 6.2. All the results reveal that the OER activity of $LiMnO_2$-Li_2MnO_3 is superior among all prepared materials and even better than commercial RuO_2.

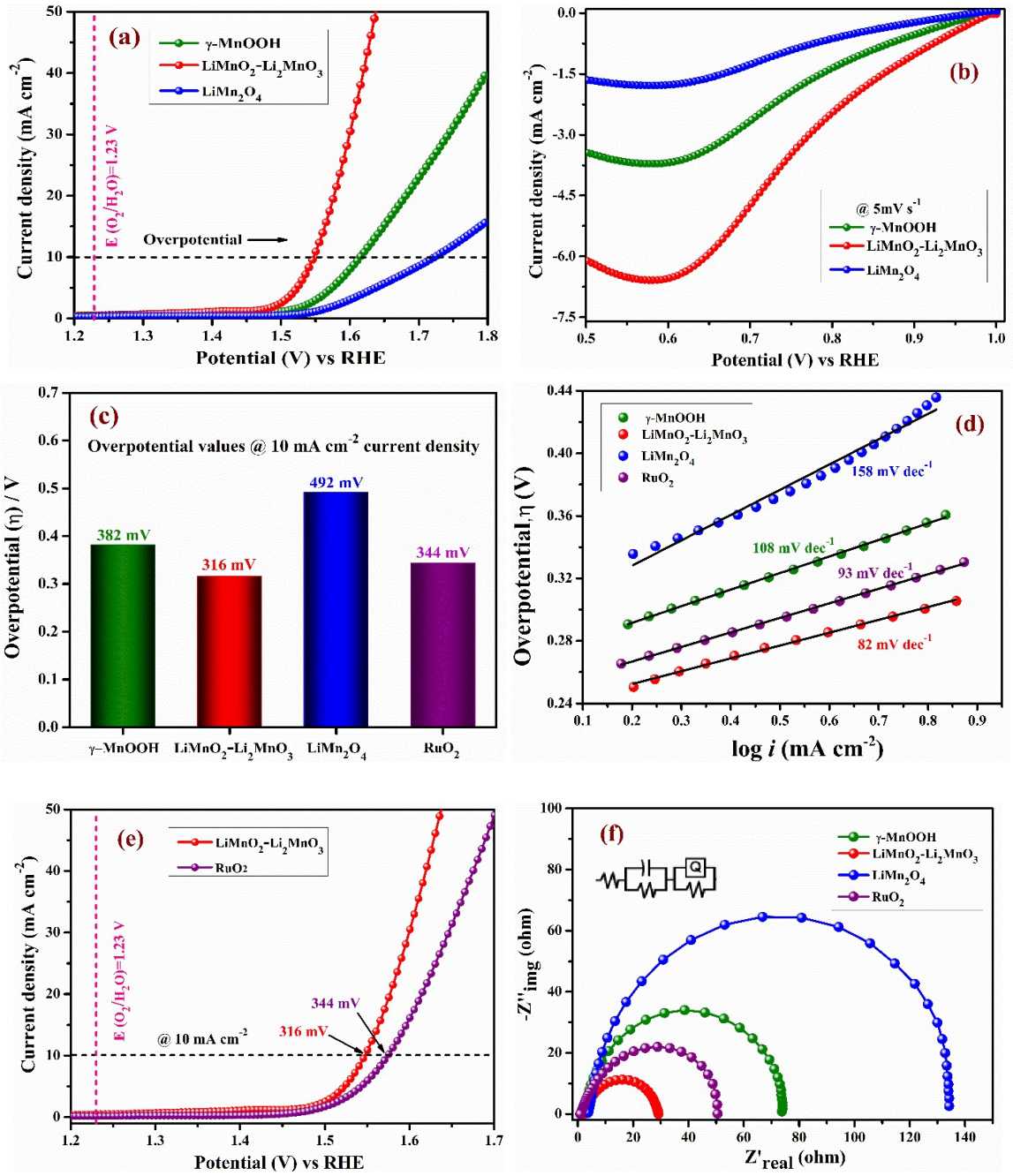

Figure 6.7: (a) LSV at a scan rate of 5 mVs^{-1} in 1 M KOH, (b) ORR activity of different catalysts, (c) overpotentials at a current density of 10 $mAcm^{-2}$, (d) Tafel plots, (e) LSV comparison $LiMnO_2$-Li_2MnO_3 and RuO_2, and (f) EIS recorded at 1.54 V vs RHE.

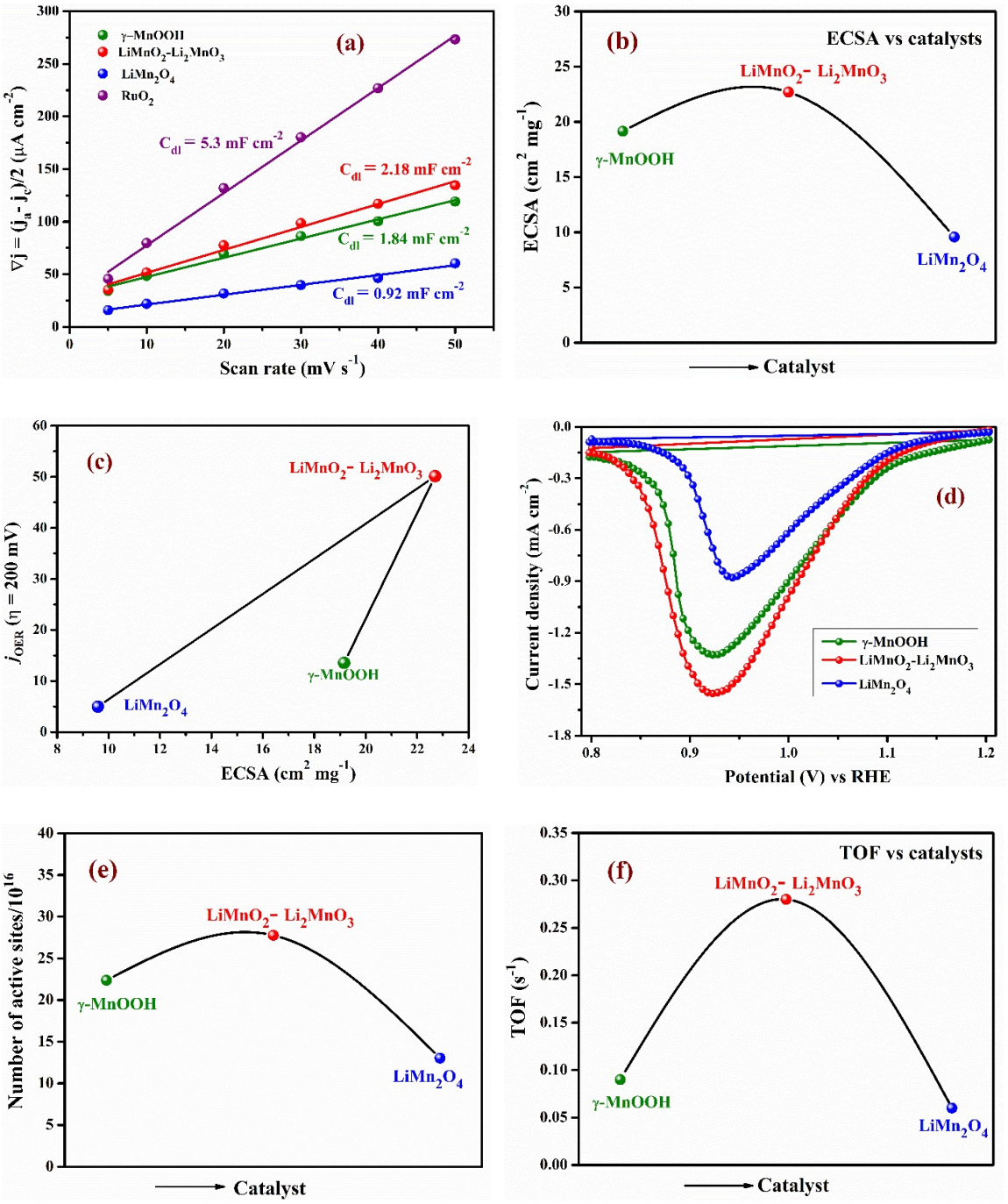

Figure 6.8: (a) C_{dl} values, (b) ECSA vs Catalyst, (c) OER attained at 200 mV overpotential vs. ECSA, (d) short CV showing the reduction peak used for active sites determination, (e) The number of active sites vs catalysts, and (f) TOF vs. catalysts.

Table 6.2: Number of active sites, overpotential, TOF, and ECSA normalized current density of different synthesized catalysts.

Catalysts	Overpotential	C_{dl}	ECSA normalized current density	No. of active sites	TOF
γ-MnOOH	382	1.84	19.16	22.37×10^{16}	0.09
$LiMnO_2$-Li_2MnO_3.	316	2.18	52	27.77×10^{16}	0.28
$LiMn_2O_4$	492	0.92	9.58	13.04×10^{16}	0.06

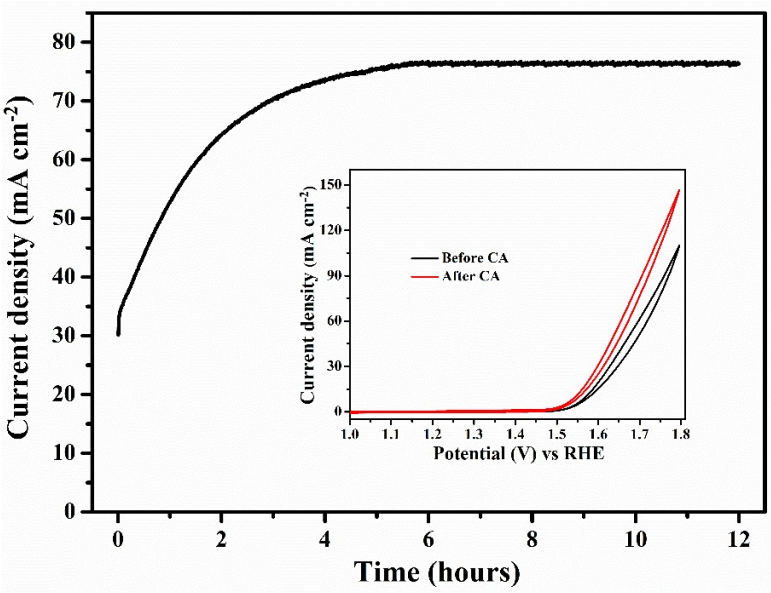

Figure 6.9: Chronoamperometric stability test of $LiMnO_2$-Li_2MnO_3 and inset showing negligible change in the CV profile taken before and after CA experiment.

Electrochemical stability is an important factor in determining the practical application of the catalyst. The static stability of $LiMnO_2$-Li_2MnO_3 was examined by performing a chronoamperometric (CA) measurement at 1.54 V vs RHE for 12 h, shown in Fig. 6.9. The CA plot indicates that $LiMnO_2$-Li_2MnO_3 nanocomposite exhibits a stable current density of 10 mA cm^{-2} that increases slightly during the first few hours; after that, it was maintained throughout the experimental time scale. In addition, the dynamic stability of $LiMnO_2$-

Li_2MnO_3 was also tested by performing a thousand cycles of CV at a scan rate of 100 mV/s in the potential range of 1.0− 1.8 V vs RHE. The inset of Fig. 6.9 shows the CV plots of the $LiMnO_2$-Li_2MnO_3 taken before and after CA experiments and it was noticed that only a marginal change in the overpotential at 10 mA cm^{-2} for $LiMnO_2$-Li_2MnO_3 nanocomposite, indicating its excellent stability in a highly alkaline 1 M KOH aqueous electrolyte.

To further explore the reason behind the high electrocatalytic activity of the catalysts, we performed CV scans in the range between 0.8 and 1.5 V vs RHE in a 1 M KOH electrolyte, shown in Figure 6.10. Previous studies have shown that the active $LiMO_2$ catalysts exhibited a pre-OER redox peak, which was attributed to in situ electrochemical lithiation of the catalyst at higher oxidation potentials [243][244]. In non-aqueous Li^+ electrolytes, $LiMO_2$ (M = Ni, Co, Cr, Mn) exhibited reversible Li^+ insertion/deinsertion in the range between 3.2 and 4.2 V vs Li/Li^+ (or 0−1 V vs Ag/AgCl) [243]. However, the behavior of $LiMO_2$ in aqueous electrolytes is less reported, but in alkaline solutions, they exhibited reversible redox peaks of M^Z/M^{Z+1} depending upon the pH of the electrolyte [243]. Hence, a lithium-rich disordered layered structure in the form of Li_2MnO_3 ($Li_{2/3}[Li_{1/3}Mn_{2/3}]O_2$) can serve as an active center for the OER process. These faradaic features depict the in-situ activation of the catalyst that is accompanied by the oxidation of Mn^{3+} to Mn^{4+}, making a Li-rich and oxygen-deficient center in the catalysts. A large number of oxygen vacancies favor more adsorption of OH^- ions on the catalyst surface and facilitate −Mn−O−OH formation. Furthermore, in strongly alkaline conditions, $LiMnO_2$-Li_2MnO_3 nanocomposite has a tendency to form Mn^{3+}-di-μ-oxo-Mn^{4+} complex, which enhances the migration of electrons due to Mn^{3+}–O^{2-}–Mn^{4+} hopping conduction. As mentioned above, the pre-OER redox peak associated with Mn^{3+}/Mn^{4+} redox couples serves as an indicator of the superiority of the $LiMnO_2$-Li_2MnO_3 composite, which shows a very low onset potential with the highest current density among all synthesized catalysts.

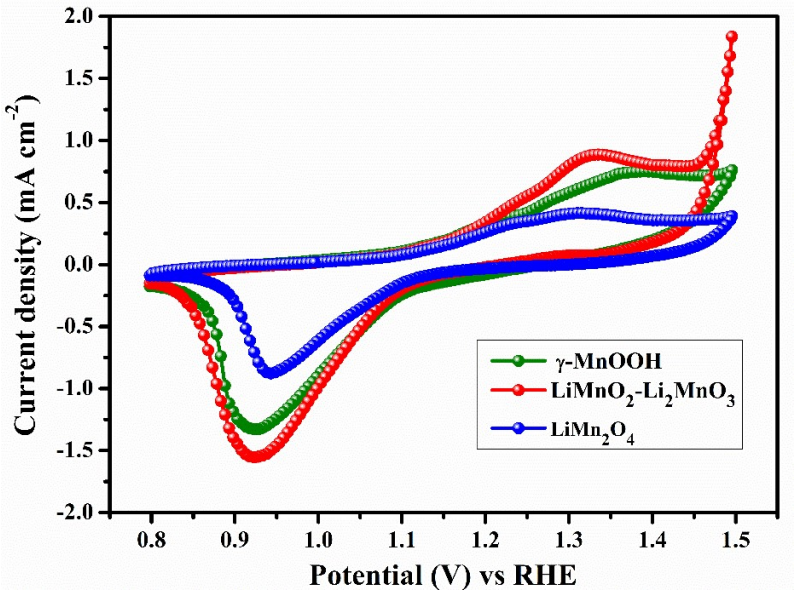

Figure 6.10: CV profiles of different synthesized catalysts showing the redox peaks for the oxidation of Mn^{III}/Mn^{IV} during the OER.

6.3.5 Post OER characterizations:

Post-OER characterizations (such as SEM and TEM) were carried out to see the effect of electrochemical cycling on the microstructure of the synthesized nanocomposite ($LiMnO_2$-Li_2MnO_3). The post-OER SEM images of the $LiMnO_2$-Li_2MnO_3 electrode reveal that the morphology is maintained even after long-term anodic cycling (Figure 6.11a). In addition, the post-OER elemental mapping images demonstrate the existence of Mn, C, and O elements in the $LiMnO_2$-Li_2MnO_3 electrode depicted in bottom of Figure 6.11a. The stability of the catalyst ($LiMnO_2$-Li_2MnO_3) was further verified through TEM and SAED analysis. Figure 6.11b shows the post-OER TEM micrograph of the electrode material, Further, the SAED pattern (Figure 6.11c) exhibits distinct diffraction spots indexed to (003), (101), (012), (104), and (015) planes, showing both phases are still preserved in the composite. This post-OER analysis confirms the stability of the catalyst that can become an alternative for efficient, cheaper, and long-lasting alternate OER catalysts for water electrolyzers.

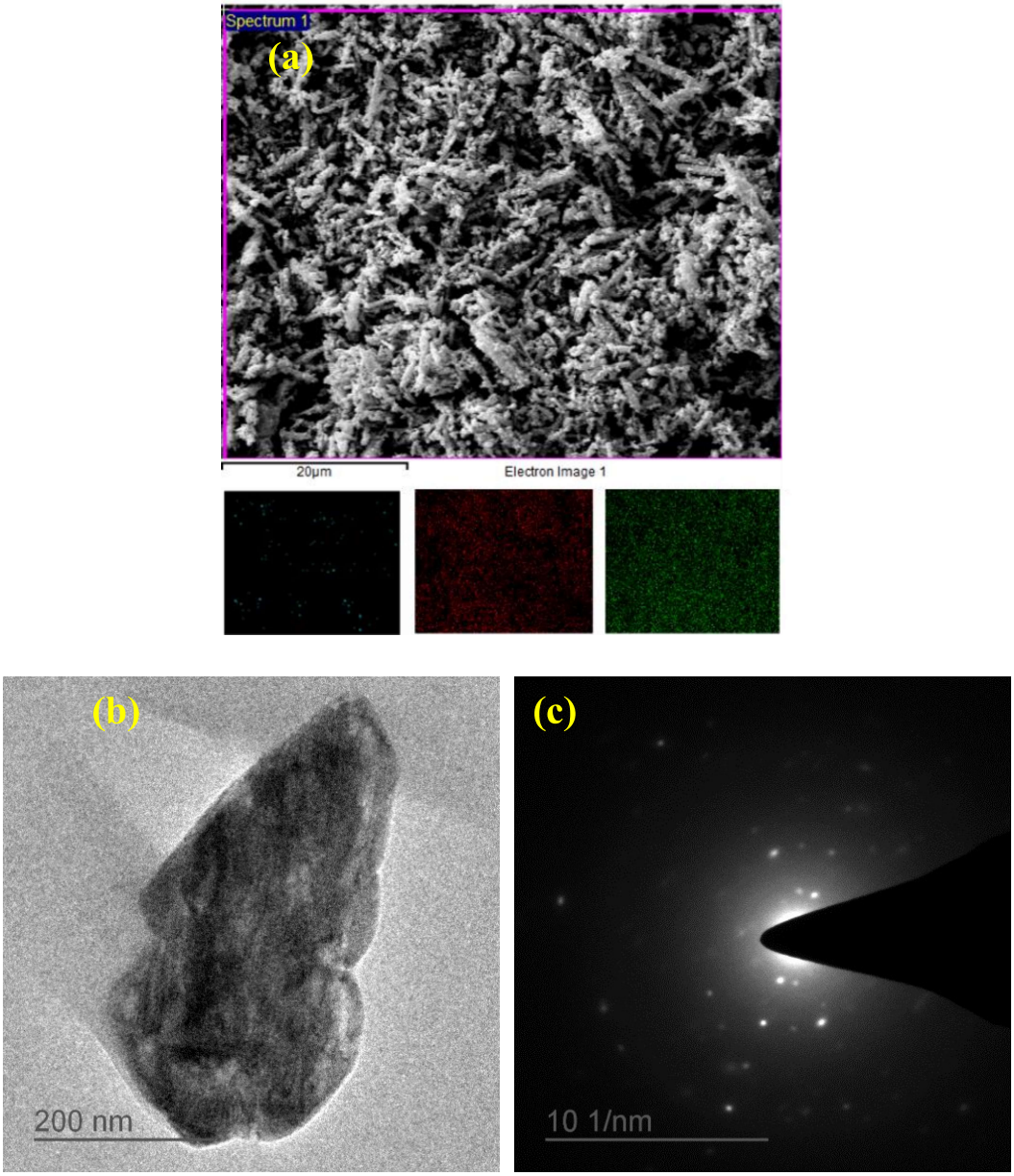

Figure 6.11: (a) post-OER SEM images of the $LiMnO_2$-Li_2MnO_3, (b) TEM, (c) SAED pattern of spent $LiMnO_2$-Li_2MnO_3.

6.4 Conclusion

In summary, different Mn-based layered compounds (γ-MnOOH, $LiMnO_2$-Li_2MnO_3, and spinel $LiMn_2O_4$) were synthesized via a simple cost-effective hydrothermal method and investigated as a bi-functional OER/ORR catalyst in 1M KOH aqueous electrolyte. XRD, Rietveld refinement, SAED pattern, and HR-TEM image clearly show that nanocomposite consisting of 56 % $LiMnO_2$ and 44% Li_2MnO_3 have a large number of structure defects such as ordered oxygen vacancies resulting in stacking faults into its structure and might be the reason behind the superior performance of composite over other synthesized catalysts. The superior OER/ORR performance was attributed in terms of a large number of surface-active sites, lower overpotential, higher turnover frequency (TOF), and low charge transfer resistance. Additionally, the presence of ordered oxygen-vacant sites may lead to the formation of terminal hydroxyl and Mn^{3+}-di-μ-oxo-Mn^{4+} complexes, which may further enhance the catalytic activity of the composite material. An optimized ratio of Mn^{3+}/Mn^{4+} in layered $LiMnO_2$-Li_2MnO_3 may be achieved through the electrochemical lithiation/de-lithiation process and offers valuable insight into developing efficient OER catalysts.